Engineered nanoplatform mediated gas therapy enhanced ferroptosis for tumor therapy *in vivo*

Kun Xu [a,c,1], Ke Li [a,b,**,1], Ye He [b], Yulan Mao [a], Xuan Li [a], Liangshuai Zhang [a], Meijun Tan [a], Yulu Yang [a], Zhong Luo [d], Peng Liu [a,***], Kaiyong Cai [a,*]

[a] *Key Laboratory of Biorheological Science and Technology, Ministry of Education College of Bioengineered, Chongqing University Chongqing, 400044, PR China*
[b] *Thomas Lord Department of Mechanical Engineered and Materials Science, Duke University, Durham, NC, 27708, USA*
[c] *Chongqing Key Laboratory for Advanced Materials and Technologies of Clean Energies, School of Materials and Energy, Southwest University, Chongqing, 400715, PR China*
[d] *School of Life Science, Chongqing University, Chongqing, 400044, PR China*

ARTICLE INFO

ABSTRACT

The high glutathione (GSH) environment poses a significant challenge for inducing ferroptosis in tumor cells, necessitating the development of nanoplatforms that can deplete intracellular GSH. In this study, we developed an engineered nanoplatform (MIL-100@Era/L-Arg-HA) that enhances ferroptosis through gas therapy. First, we confirmed that the Fe element in the nanoplatform undergoes valence changes under the influence of high GSH and H_2O_2 in tumor cells. Meanwhile, L-Arg generates NO gas in the presence of intracellular H_2O_2, which reacts with GSH. Additionally, Erastin depletes GSH by inhibiting the cystine/glutamate antiporter system, reducing cystine uptake and impairing GPX4, while also increasing intracellular H_2O_2 levels by activating NOX4 protein expression. Through these combined GSH-depletion mechanisms, we demonstrated that MIL-100@Era/L-Arg-HA effectively depletes GSH levels, disrupts GPX4 function, and increases intracellular lipid ROS levels *in vitro*. Furthermore, this nanoplatform significantly inhibited tumor cell growth and extended the survival time of tumor-bearing mice *in vivo*. This engineered nanoplatform, which enhances ferroptosis through gas therapy, shows significant promise for ferroptosis-based cancer therapy and offers potential strategies for clinical tumor treatment.

1. Introduction

The high glutathione (GSH) environment within tumor cells poses a significant challenge for inducing ferroptosis, a type of iron-dependent programmed cell death characterized by the accumulation of lipid reactive oxygen species (ROS) [1–4]. GSH, as a crucial antioxidant, maintains cellular redox balance by reducing lipid peroxides and inhibiting the accumulation of lipid ROS, thereby preventing ferroptosis [5,6]. These elevated GSH levels reduce the effectiveness of ferroptosis-based therapies, underscoring the need for innovative strategies to effectively deplete GSH and enhance therapeutic outcomes.

Consequently, elevated GSH levels within tumor cells reduce the efficacy of therapies aimed at inducing ferroptosis, necessitating strategies to deplete GSH for successful therapeutic outcomes [7,8]. Recent research has demonstrated that nanomaterial-based systems, through intrinsic material properties or surface modifications, can effectively reduce intracellular GSH levels [9–11]. For instance, nanoparticles such as iron-based metal-organic frameworks (MOFs) have been designed to consume GSH during catalytic reactions, thereby promoting the induction of ferroptosis [12–14]. These strategies highlight the importance of developing novel nanomaterials that can deplete GSH and enhance cancer cell sensitivity to ferroptosis (see Scheme 1).

Scheme 1. Schematic illustration of the engineered nanoplatforms mediating gas therapy to enhance ferroptosis for tumor therapy. (A) The synthesis process of MIL-100@Era/L-Arg-HA. (B) The released Erastin increases intracellular H_2O_2 levels and reduces GSH levels by inhibiting the system Xc−. Fe^{3+} in the nanoplatform reacts with intracellular GSH to generate Fe^{2+}, inducing ferroptosis. Additionally, Fe^{2+} further reacts with H_2O_2 to regenerate Fe^{3+}. L-Arg catalyzes the production of NO inside the cell, and NO subsequently consumes GSH through biocatalysis, producing GSSG. These mechanisms collectively deplete intracellular GSH, reduce GPX4 protein levels, and increase intracellular Lipid ROS. The combined effects of gas therapy and ferroptosis ultimately lead to cell death.

Beyond ferroptosis, combining this mechanism with other therapeutic approaches such as immunotherapy, photothermal therapy (PTT), and gas therapy has shown synergistic potential in tumor treatment [15–19]. Infiltrating CD8+ T cells secrete IFN γ cytokines that downregulate the expression of the cystine transporter on tumor cell surfaces, thereby enhancing lipid peroxidation and ferroptosis in tumor cells [20]. Zhang et al. reported the construction of nanomotors by co-loading hemin and ferrocene (Fc) on the surface of bowl-shaped polydopamine (PDA) nanoparticles. Due to the photothermal effect of PDA, it can enhance ROS production, thereby interfering with the Fenton reaction process and achieving photothermally enhanced ferroptosis [21]. Combining gas therapy with ferroptosis has unique advantages in depleting GSH and improving therapeutic efficacy. Cao et al. found that carbon monoxide(CO) triggered ferroptosis by modulating the ROS/GSK3β/GPX4 signaling pathway, resulting in the accumulation of lipid hydroperoxides and the occurrence of ferroptosis [22]. These combined strategies demonstrate the potential of leveraging multiple mechanisms to effectively induce ferroptosis in tumor cells.

Based on these advancements, we developed a novel nanoplatform that enhances ferroptosis through gas therapy. This nanoplatform depletes intracellular GSH levels in tumor cells through multiple mechanisms. In brief, this engineered nanoplatform utilizes MIL-100 nanoparticles loaded with the ferroptosis activator Erastin and surface-modified with L-arginine (L-Arg) and hyaluronic acid (HA). The MIL-100@Era/L-Arg-HA nanoplatform promotes intracellular GSH depletion and NO production, synergistically inducing ferroptosis in tumor cells. The Fe element contained in MIL-100 undergoes valence changes between Fe^{3+} and Fe^{2+} under the action of GSH and H_2O_2. L-Arg, catalyzed by intracellular H_2O_2 and other substances, produces NO gas that reacts with GSH. Erastin inhibits the cystine/glutamate antiporter system to deplete GSH, thereby reducing cystine uptake and impairing GPX4, while also increasing intracellular H_2O_2 levels by activating NOX4 protein expression. We hypothesize that these combined mechanisms can maximally deplete intracellular GSH levels, reduce GPX4 levels, and ultimately activate ferroptosis. This gas therapy-enhanced ferroptosis nanoplatform not only effectively depletes GSH and increases lipid ROS levels but also represents a promising therapeutic strategy for treating tumors in high GSH environments.
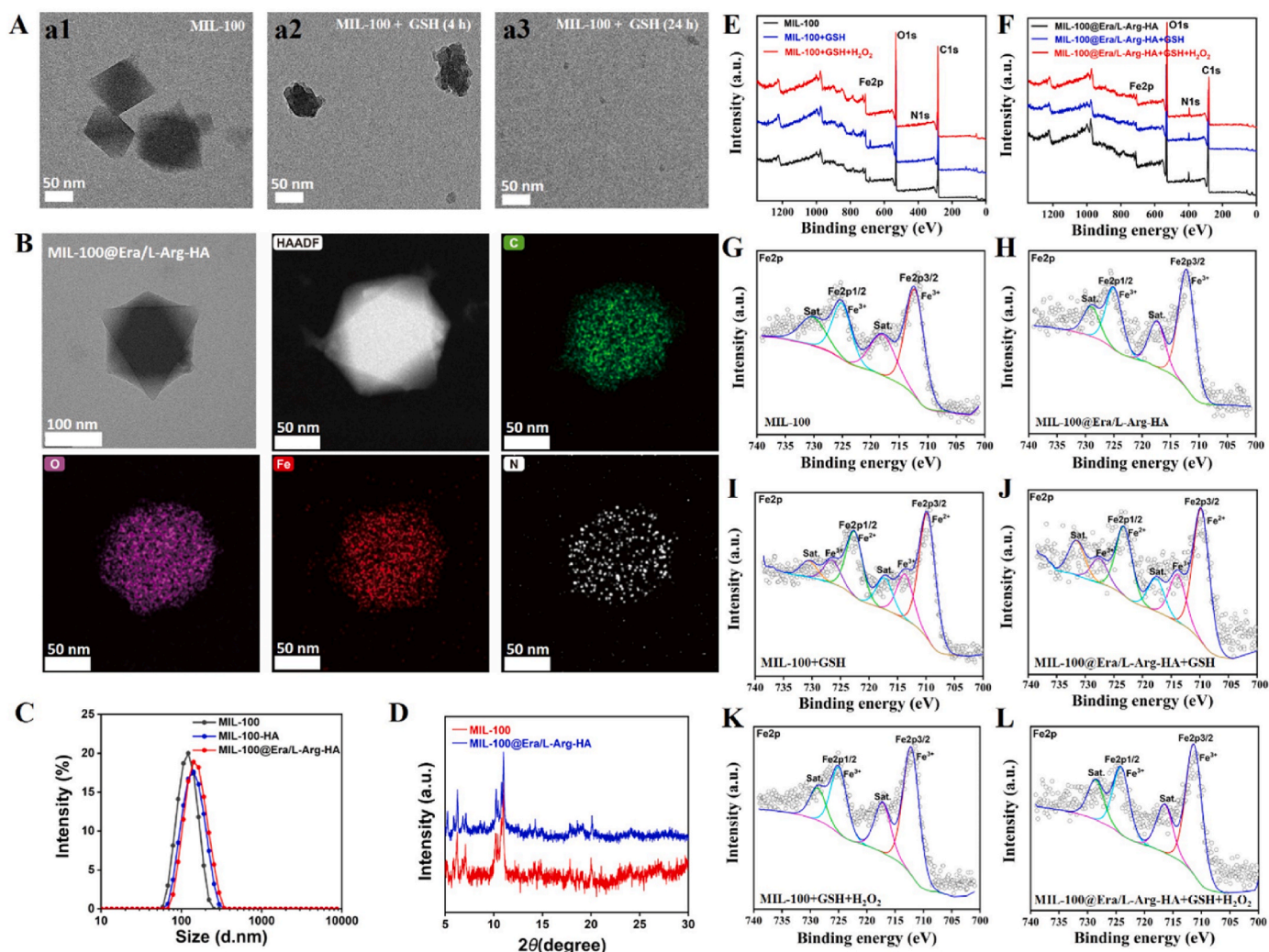
Fig. 1. **Synthesis and characterization of engineered nanoplatform.** (A) TEM images of MIL-100 nanoparticles; (B) The TEM and corresponding mapping of MIL-100@Era/L-Arg-HA; (C) DLS of MIL-100, MIL-100-HA and MIL-100@Era/L-Arg-HA; (D) The XRD patterns of MIL-100 and MIL-100@Era/L-Arg-HA; (E) The XPS spectrum of MIL-100 NPs reaction with GSH and H_2O_2; (F) The XPS spectrum of MIL-100@Era/L-Arg-HA NPs reaction with GSH and H_2O_2; (G–L) XPS spectra of Fe elements before and after the reaction of MIL-100 and MIL-100@Era/L-Arg-HA with GSH and H_2O_2.

2. Results and discussion

2.1. Preparation and characterization of engineered nanoplatforms

The schematic for synthesizing the engineered nanoplatforms is shown in Fig. 1A. Based on previous literature [23,24], we successfully synthesized MIL-100 nanoparticles. As shown in Fig. 1A–a1 and **S1**, we successfully synthesized MIL-100 nanoparticles with uniform morphology. To enhance the ferroptosis-inducing capability of the nanoplatforms, we loaded the ferroptosis activator Erastin into the nanoparticles. Subsequently, to introduce L-Arg and targeting groups, we engineered the surface of MIL-100 with dopamine-hyaluronic acid (DPA-HA). As shown in Fig. S2, we successfully synthesized the DPA-HA polymer. Meanwhile, as shown in Fig. S3, after loading Erastin and DPA-HA, there was a slight change in the surface charge of the nanoparticles. Upon introducing L-Arg, the overall charge of the nanoplatforms changed from −24.67 mV to approximately −21 mV due to the positive charge of L-Arg. Additionally, the hydrodynamic diameter of MIL-100 changed slightly after different surface modifications: MIL-100-HA had a hydrodynamic diameter of 140 nm, and MIL-100@Era/L-Arg-HA had a diameter of approximately 160 nm. To further characterize the impact of surface functionalization on morphology, we performed TEM characterization of the engineered

nanoplatforms. As shown in Fig. 1B, there was no significant change in the overall morphology of the nanoplatforms after surface functionalization, but the corresponding EDS mapping results indicated the appearance of a new N element. And the dynamic light scattering (DLS) test results also showed that after surface modification, the hydrodynamic diameter showed a slight increasing trend (Fig. 1C). To further characterize the changes in the nanoplatforms during the synthesis process, we employed X-ray powder diffraction (XRD) and X-ray photoelectron spectroscopy (XPS). These techniques allowed us to investigate alterations in the crystal form and elemental composition of the nanoparticles throughout the material synthesis. As shown in Fig. 1D, there was no significant change in the nanocrystal form of MIL-100 before and after surface functionalization, which is consistent with previous reports in the literature [25]. As shown in Fig. 1E and **F**, the MIL-100@Era/L-Arg-HA exhibited very distinct N element characteristic peaks after surface functionalization. As shown in Fig. S4, we found that the nanoplatform exhibits excellent stability under physiological conditions, maintaining good morphology and uniform hydrodynamic diameter even after 3 days in PBS solution. Additionally, to further verify the valence state changes of Fe elements in the engineered nanoplatforms within the intracellular physiological environment of tumor cells, we simulated the high GSH and H_2O_2 environment of tumor cells. MIL-100 and MIL-100@Era/L-Arg-HA were exposed to PBS buffer
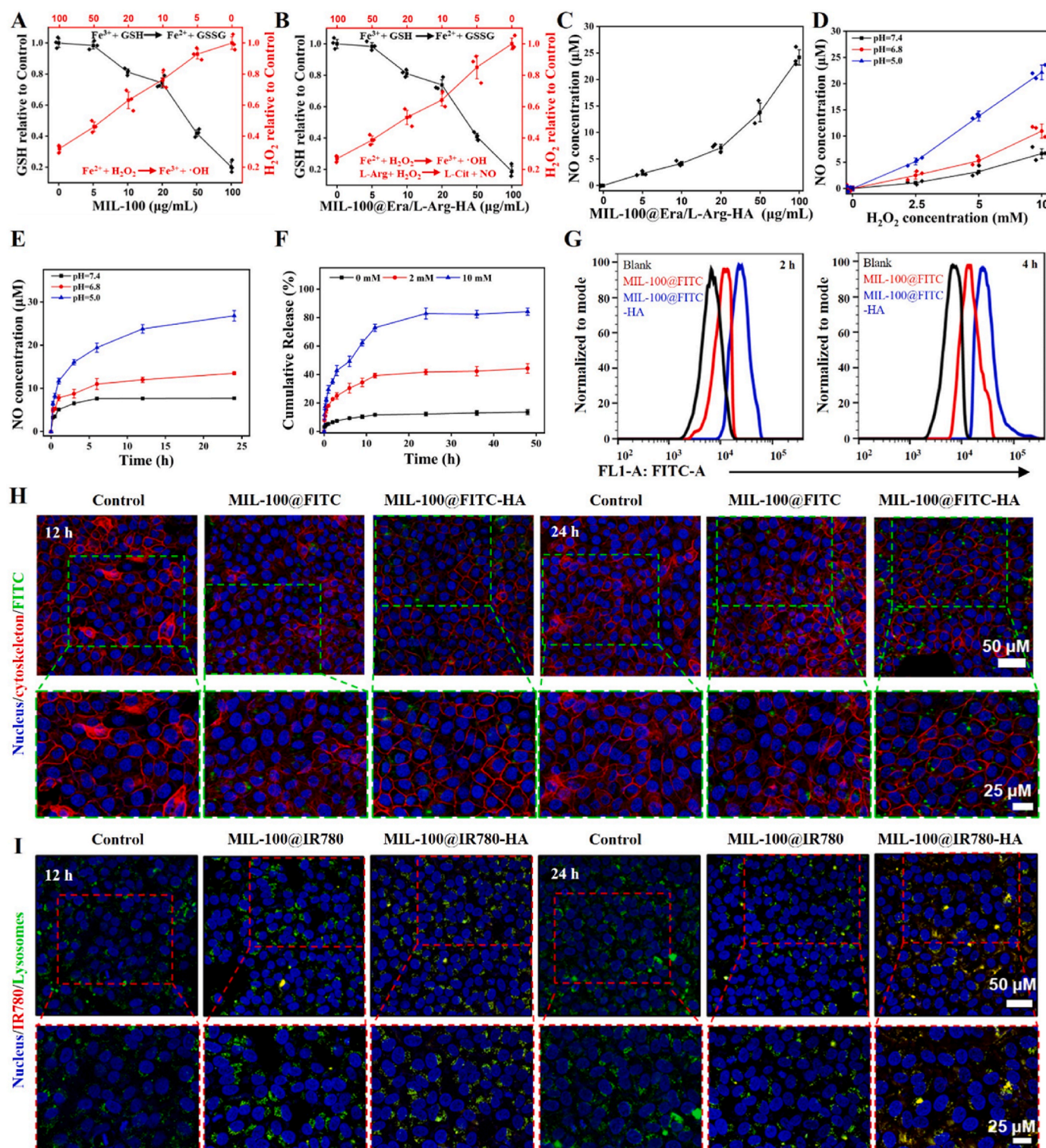
Fig. 2. Characterization of the catalytic performance of the nanoplatform and HA-mediated cell targeting. (A) The ability of various concentration of MIL-100 NPs to deplete GSH and H_2O_2 in solution; (B) The ability of various concentration of MIL-100@Era/L-Arg-HA to deplete GSH and H_2O_2 in solution; (C) The NO generation capability of MIL-100@Era/L-Arg-HA at different concentrations; (D) NO generation capability under different pH and H_2O_2 conditions; (E) The ability of MIL-100@Era/L-Arg-HA generate NO over time under different pH conditions; (F) Drug release profile of Erastin under different pH conditions; (G) Flow cytometry analysis of the cellular uptake efficiency of the HA-mediated targeting; (H) CLSM detection of tumor cell phagocytosis of the nanoplatform; (I) CLSM detection of colocalization between the nanoplatform and lysosomes in tumor cells.

solutions containing the same concentrations of GSH and H_2O_2. Samples were then collected and characterized for the valence state of Fe elements after the reaction. As shown in Fig. 1G and **H**, Fe elements in MIL-100 and MIL-100@Era/L-Arg-HA were initially present as Fe^{3+}.

After exposure to the GSH environment, the Fe elements in MIL-100 and MIL-100@Era/L-Arg-HA predominantly shifted to Fe^{2+}, with a small amount of Fe^{3+} still present. Upon further addition of H_2O_2, the valence state of the Fe elements primarily reverted to Fe^{3+}, with a very small
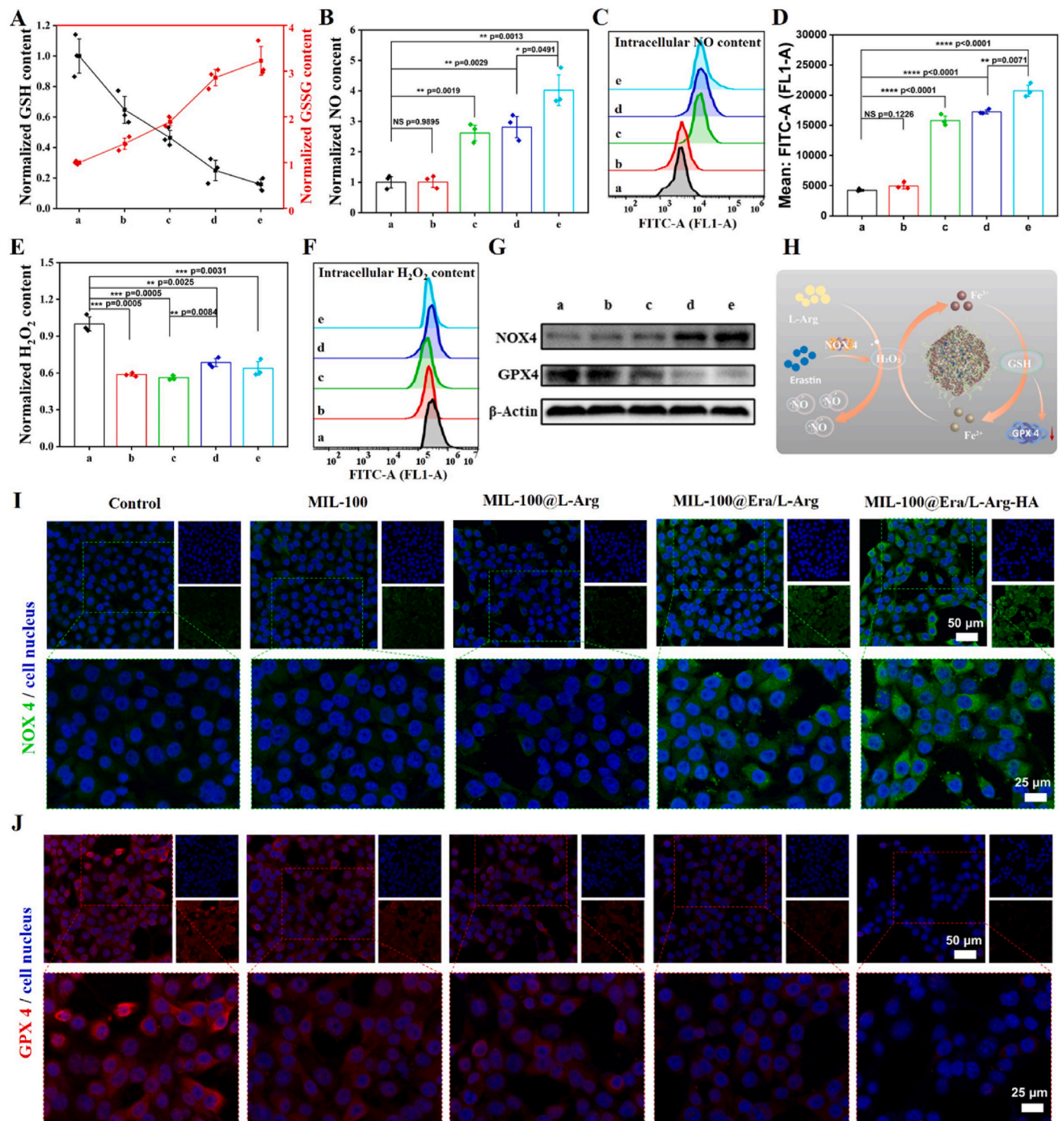
Fig. 3. Evaluation of the intracellular catalytic performance of the nanoplatform. (A) Changes in intracellular GSH and GSSG levels after treatment with different nanoplatforms; (B) Changes in intracellular NO levels after treatment with different nanoplatforms; (C) Changes in NO levels detected by flow cytometry after treatment with different nanoplatforms; (D) Flow cytometry results of NO levels and corresponding fluorescence value statistics; (E) Changes in intracellular H_2O_2 levels after different treatments; (F) Changes in H_2O_2 levels detected by flow cytometry after treatment with different nanoplatforms; (G) Western Blotting detecting the NOX4 and GPX4 protein expression levels with different treatment (In Fig. 3A–G, a is Control, b is MIL-100, c is MIL-100@L-Arg, d is MIL-100@Era/L-Arg, and e is MIL-100@Era/L-Arg-HA); (H) Schematic illustration of intracellular catalysis by the engineered nanoplatform; (I) Immunofluorescence staining of NOX4 protein; (J) Immunofluorescence staining of GPX4 protein. All data were processed in GraphPad software (GraphPad Prism version 8.0 for Windows) by *t*-test (n = 3). The significance of difference was determined *via t*-test. *p < 0.05, **p < 0.01, ***p < 0.001, ****p < 0.0001.

amount of Fe^{2+} remaining. In short, we successfully surface modified MIL-100 while ensuring its ability to facilitate the valence state changes of Fe elements between Fe^{2+} and Fe^{3+} within the physiological environment of tumor cells.

2.2. Catalytic performance characterization of engineered nanoplatforms

We used GSH and H_2O_2 assay kits to characterize the ability of the engineered nanoplatforms to react with GSH and H_2O_2. As shown in Fig. 2A, with the increase in nanoparticle concentration, the concentration of GSH in the solution gradually decreased. This is because Fe^{3+} in MIL-100 reacts with GSH to generate Fe^{2+} and GSSG, thereby consuming the GSH in the solution. Meanwhile, with the increase in nanoparticle concentration, the concentration of H_2O_2 in the solution also gradually decreased. This is due to the reaction of Fe^{2+} with H_2O_2, resulting in the generation of Fe^{3+}. This also corroborates the changes in the valence state of Fe elements obtained from the XPS analysis. MIL-100@Era/L-Arg-HA produced similar experimental results (Fig. 2B), consistent with the XPS analysis, indicating that surface functionalization and drug loading on MIL-100 did not affect its ability to react with GSH and H_2O_2. However, due to the presence of L-Arg, which can react with H_2O_2 to produce NO, MIL-100@Era/L-Arg-HA exhibited a stronger reaction capacity with H_2O_2. This was consistent with the previous report [26]. Therefore, at the same nanoparticle concentration, the H_2O_2 concentration in the MIL-100@Era/L-Arg-HA group was lower than that in the MIL-100 group.

To further characterize the H_2O_2 generation ability of MIL-100@Era/L-Arg-HA, we used a NO assay kit to detect its NO production capacity. We exposed MIL-100@Era/L-Arg-HA to a solution containing H_2O_2. As shown in Fig. 2C, the amount of NO generated increased with the concentration of MIL-100@Era/L-Arg-HA nanoparticles. Fig. 2D shows that at different pH values, the amount of NO generated increased with the concentration of H_2O_2 in the buffer. Additionally, as the pH decreased, the amount of NO generated increased at the same H_2O_2 concentration. This is because the HA modification protects L-Arg, and the L-Arg modification on the nanoparticle surface mainly relies on electrostatic adsorption and Schiff base reactions [27]. Both mechanisms weaken in acidic environments, releasing L-Arg from the MIL-100 surface and accelerating its reaction with H_2O_2 to produce NO. As shown in Fig. 2E, when the H_2O_2 concentration in the buffer was 10 mM, the amount of NO produced by MIL-100@Era/L-Arg-HA reaches its maximum within 24 h.

2.3. Evaluation of Erastin release behavior

As reported in previous literature [28,29], MIL-100 nanoparticles undergo slow degradation in the presence of GSH, releasing the loaded drug. To verify the release performance of Erastin, we dispersed MIL-100@Era/L-Arg-HA in PBS buffer solutions with different concentrations of GSH. As shown in Fig. 2F, at a GSH concentration of 10 mM, the cumulative release of Erastin reached 84.26 % within 24 h. In contrast, at a GSH concentration of 2 mM, the cumulative release of Erastin was only 44.28 %, while at a GSH concentration of 0 mM, the cumulative release was merely 13.65 %. This phenomenon is consistent with the morphological changes of MIL-100 exposed to GSH solutions shown in Fig. 1A–a2 and **a3**. This indicates that in the high-GSH physiological environment of tumor cells, Erastin can be released from MIL-100@Era/L-Arg-HA, thereby activating ferroptosis.

2.4. Evaluation of tumor targeting effect of engineered nanoplatforms

Hyaluronic acid (HA) is a naturally occurring polysaccharide in human tissues, with receptors such as CD44 and RHAMM highly expressed on many types of tumor cells, especially on the surface of breast tumor cell membranes [30–32]. Here, we selected 4T1 tumor cells as the cell line to study the engineered nanoplatforms. To better assess

the targeting effect of the engineered nanoplatforms, we evaluated the phagocytosis behavior of 4T1 tumor cells over different time periods using flow cytometry and CLSM. As shown in Fig. 2G, HA-modified nanoplatforms were taken up more by 4T1 cells compared to the non-HA modified group. The corresponding quantitative fluorescence statistical results (Fig. S4) also confirmed that 4T1 cells incubated with the HA-modified nanoplatforms showed higher fluorescence values. To visually evaluate the phagocytosis behavior of tumor cells, we performed fluorescence imaging on differently treated cells using CLSM. As shown in Fig. 2H, the MIL-100@FITC-HA group exhibited more green fluorescence, indicating that HA-mediated tumor targeting effect facilitated the phagocytosis of the nanoplatforms by tumor cells. Additionally, to further characterize the intracellular distribution of the nanoplatforms after being phagocytosed by tumor cells, we conducted fluorescence imaging of the lysosomes in tumor cells. As shown in Fig. 2I, the nanoplatforms were widely distributed within the lysosomes of tumor cells after phagocytosis, thereby exerting the effect of activating ferroptosis.

2.5. Evaluation of intracellular catalytic activity with engineered nanoplatforms treatment

In previous experiments, we verified that the Fe element within the nanoplatforms could effectively convert between Fe^{3+} and Fe^{2+} ions in the presence of GSH and H_2O_2, thereby consuming intracellular GSH. To further evaluate the interaction of the nanoplatforms with GSH and H_2O_2 in tumor cells, we first characterized the GSH and GSSG levels in tumor cells after different treatments using GSH and GSSG assay kits. As shown in Fig. 3A, the GSH level in the MIL-100 group significantly decreased compared to the Control group. Interestingly, the GSH level in the MIL-100@L-Arg group was lower than that in the MIL-100 group, which we speculate is due to the catalytic conversion of L-Arg to NO within tumor cells. NO further consumes intracellular GSH, producing GSSG. The GSH level in the MIL-100@Era/L-Arg group was lower than that in the MIL-100@L-Arg group, likely because the introduction of Erastin increased intracellular H_2O_2 levels, facilitating the valence state conversion of Fe elements and maximally consuming intracellular GSH. The MIL-100@Era/L-Arg-HA group exhibited the lowest GSH level, likely due to the HA-mediated increase in nanoparticle uptake by tumor cells, leading to maximum intracellular GSH consumption. Consequently, the intracellular GSSG level showed an opposite trend to GSH, indicating that Fe^{3+} ions and the generated NO within the nanoplatforms consumed GSH and produced GSSG.

We further characterized the NO production capacity of the nanoplatforms within cells using a NO assay kit. As shown in Fig. 3B, intracellular NO levels significantly increased with the introduction of L-Arg, with no significant difference between the MIL-100@L-Arg and MIL-100@Era/L-Arg groups, while the MIL-100@Era/L-Arg-HA group exhibited the highest NO level. To more accurately characterize NO content, we used a NO green fluorescent probe. As shown in Fig. 3C and **D**, flow cytometry results indicated that the MIL-100@Era/L-Arg-HA group exhibited the highest green fluorescence intensity, consistent with the NO assay kit results. Since H_2O_2 is a key component for the valence state conversion of Fe^{3+} and Fe^{2+} ions within the nanoplatforms, we also characterized its content using H_2O_2 assay kits and flow cytometry. As shown in Fig. 3E–G, the MIL-100 and MIL-100@L-Arg groups exhibited lower H_2O_2 levels compared to the Control group, while the MIL-100@Era/L-Arg and MIL-100@Era/L-Arg-HA groups showed higher H_2O_2 levels than the MIL-100 and MIL-100@L-Arg groups. We speculate that the introduction of Erastin increased intracellular NOX4 protein expression, thereby raising intracellular H_2O_2 levels.
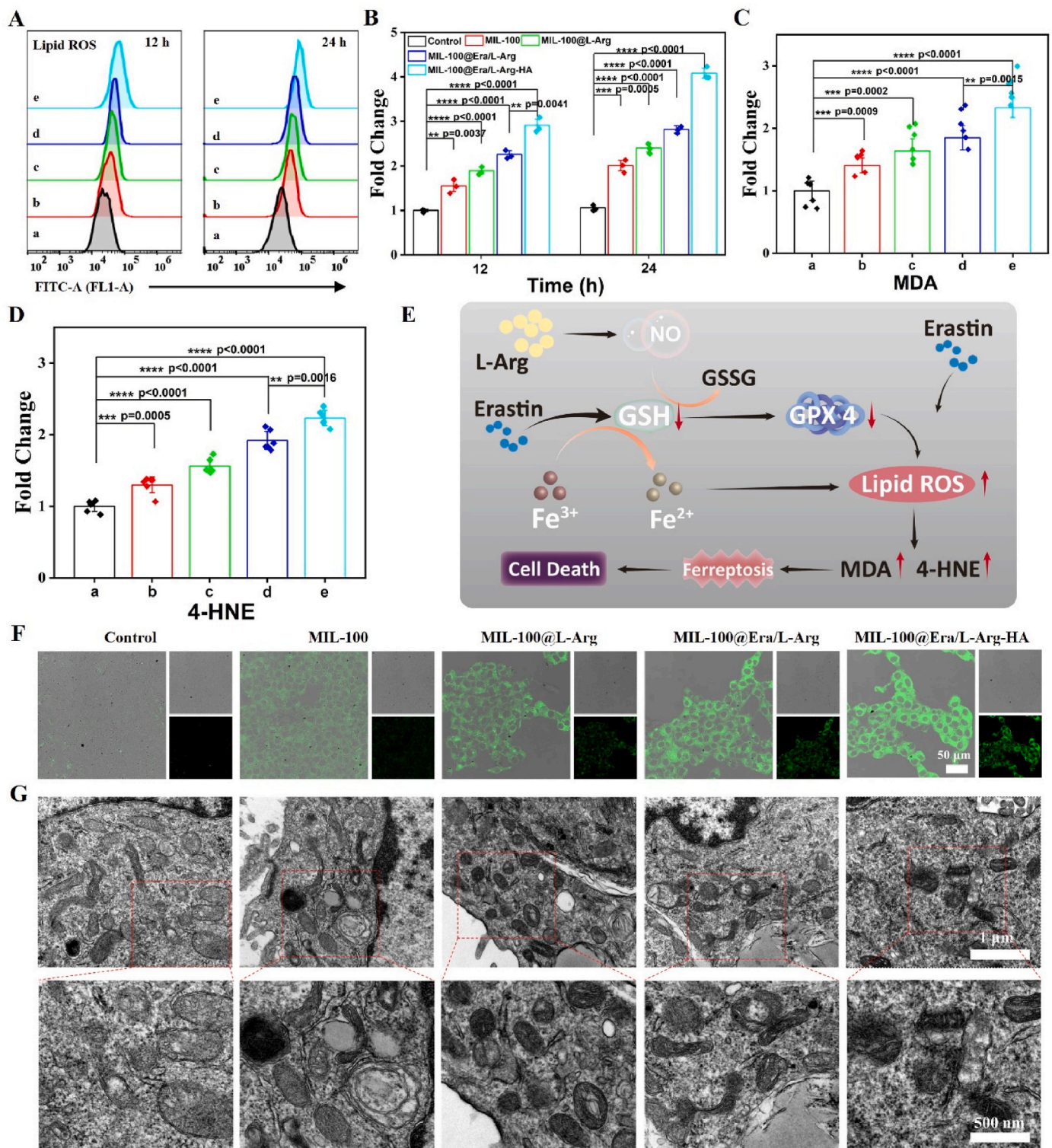
Fig. 4. Evaluation of the ferroptosis-inducing capability of the engineered nanoplatform. (A) Flow cytometry detection of intracellular Lipid ROS levels (a is Control, b is MIL-100, c is MIL-100@L-Arg, d is MIL-100@Era/L-Arg, and e is MIL-100@Era/L-Arg-HA); (B) Fluorescence value statistics from flow cytometry results corresponding to Lipid ROS levels; (C) Changes in MDA levels within tumor cells after treatment with different nanoplatforms; (D) Changes in 4-HNE levels within tumor cells after treatment with different nanoplatforms; (E) Schematic illustration of the mechanism by which the engineered nanoplatform activates ferroptosis; (F) CLSM detection of intracellular distribution of Lipid ROS after treatment with different nanoplatforms; (G) TEM characterization of mitochondrial morphology in tumor cells after treatment with different nanoplatforms. All data were processed in GraphPad software (GraphPad Prism version 8.0 for Windows) by *t*-test (n = 6). The significance of difference was determined *via t*-test. *p < 0.05, **p < 0.01, ***p < 0.001, ****p < 0.0001.
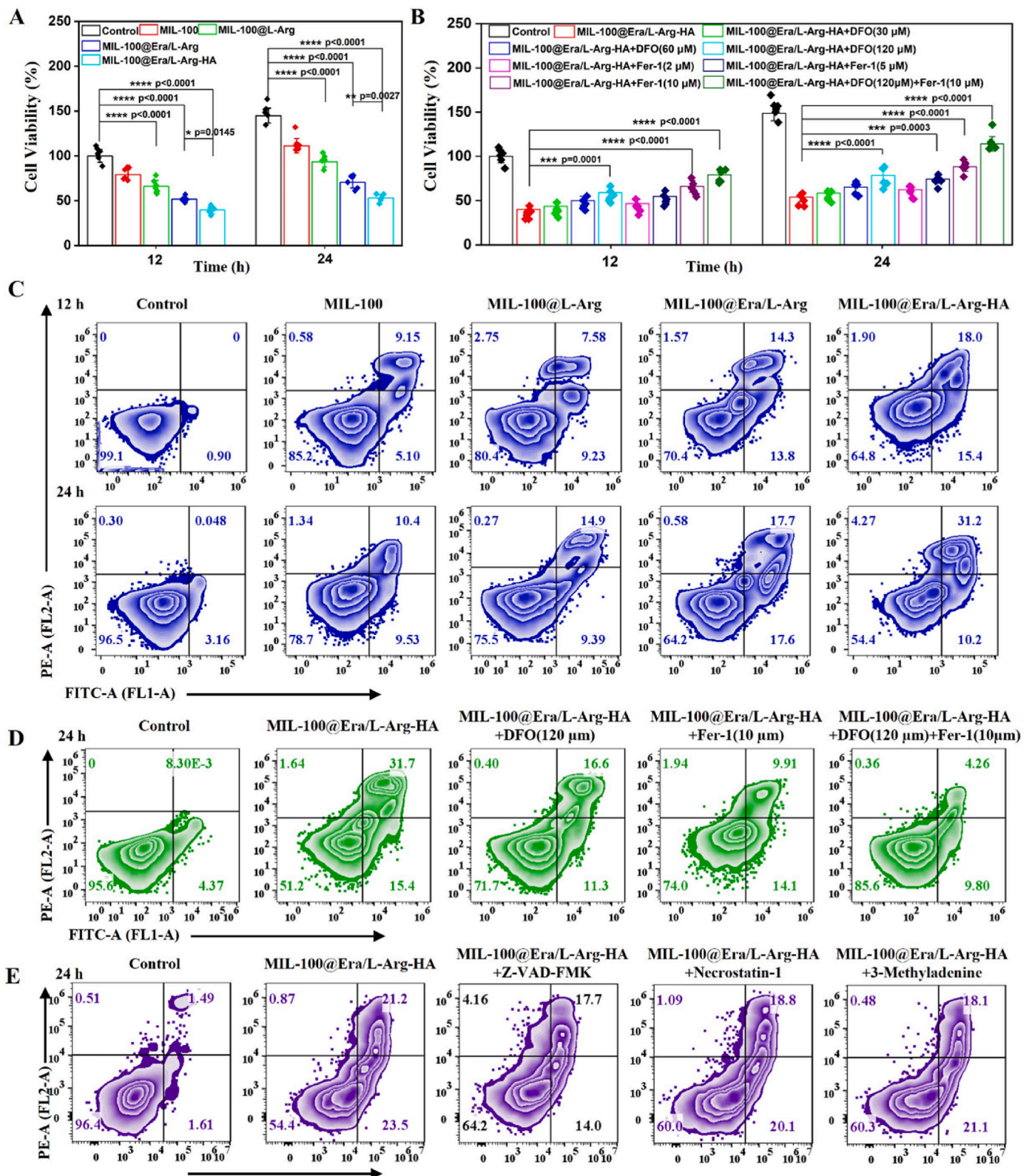
Fig. 5. Evaluation of the cell death-inducing capability of the engineered nanoplatform and the rescue effect of ferroptosis inhibitors. (A) CCK-8 assay of tumor cell viability after different treatments; (B) CCK-8 assay of cell viability after rescue with different concentrations of DFO and Fer-1 following MIL-100@Era/L-Arg-HA treatment; (C) Flow cytometry detection of cell death levels after treatment with different nanoplatforms; (D) Flow cytometry detection of cell death levels after rescue with DFO and Fer-1 following MIL-100@Era/L-Arg-HA treatment. (E) Flow cytometry detection of cell death levels after treated with Z-VAD-FMK, Necrostatin-1 and 3-Merhyladenine following MIL-100@Era/L-Arg-HA treatment. All data were processed in GraphPad software (GraphPad Prism version 8.0 for Windows) by t-test (n = 6). The significance of difference was determined *via* t-test. *$p < 0.05$, **$p < 0.01$, ***$p < 0.001$, ****$p < 0.0001$.

2.6. Evaluation of the impact of nanoplatforms on the expression of GPX4 and NOX4

NADPH oxidase 4 (NOX4) is a member of the NOX family that generates H_2O_2 by catalyzing the transfer of electrons from NADPH to O_2 [33,34]. Since the activity of NOX4 is primarily regulated by its concentration, Erastin-induced upregulation of NOX4 is expected to increase the intracellular H_2O_2 concentration [35,36], thereby facilitating the reaction with Fe^{2+} ions in the nanoplatforms. To monitor the expression levels of NOX4 protein after reaction with the nanoplatforms, Western Blotting and immunofluorescence experiments were constructed. As shown in Figs. 3G and S8A, the introduction of Erastin into the nanoplatform effectively increases NOX4 protein expression. Moreover, as shown in Figs. 3I and S9A, the green fluorescence values in the groups with Erastin-incorporated nanoplatforms (MIL-100@Era/L-Arg and MIL-100@Era/L-Arg-HA) were significantly higher than those in the other groups (control group, MIL-100 group, MIL-100@L-Arg group). This confirms our hypothesis that Erastin can enhance the expression of NOX4 protein, helping the nanoplatforms increase intracellular H_2O_2 and thus maximally deplete intracellular GSH. Intracellular glutathione (GSH) is the primary reductant for GPX4, reducing its oxidized form back to the active form, thereby allowing GPX4 to continue its antioxidant function [37,38]. Numerous studies have shown that intracellular GSH levels are related to GPX4 expression [39–41]. By reducing intracellular GSH levels, the expression of GPX4 protein can be decreased, leading to an increase in intracellular lipid reactive oxygen species, thereby activating ferroptosis. In previous experiments, we have confirmed that engineered nanoplatforms can significantly reduce intracellular GSH levels. As shown in Figs. 3G and S8B, compared to the control group, the GPX4 protein expression level in tumor cells treated with the MIL-100 group was significantly reduced. Due to the production of NO gas, the expression level in the MIL-100@L-Arg group was lower than that of the MIL-100 group. Additionally, the introduction of HA and Erastin elevated intracellular H2O2 levels, leading to maximum consumption of intracellular GSH. The MIL-100@Era/L-Arg-HA group exhibited the lowest GPX4 protein expression level, indicating that MIL-100@Era/L-Arg-HA can maximally deplete GSH and reduce GPX4 protein expression. As shown in Figs. 3J and S9B, the expression level of GPX4 in tumor cells treated with the MIL-100 group was significantly lower in red fluorescence compared to the control group. MIL-100@Era/L-Arg-HA group exhibited the lowest red fluorescence values. Those trends were consistent with the Western blotting results. Those results demonstrated that MIL-100@Era/L-Arg-HA can maximally deplete GSH and reduce the expression of GPX4 protein.

2.7. Evaluating the ferroptosis activation behavior of the engineered nanoplatforms

It is well-known that depleting intracellular GSH levels and introducing ferroptosis agonists can effectively induce ferroptosis in tumor cells [42,43]. To evaluate the ferroptosis activation capability of these engineered nanoplatforms, we first characterized the intracellular levels of lipid reactive oxygen species (ROS). As shown in Fig. 4A, after treatment with different nanoplatforms, the intracellular lipid ROS levels significantly increased compared to the control group. Among these, the lipid ROS levels in tumor cells treated with MIL-100@Era/L-Arg-HA were the highest. Corresponding fluorescence value statistics also indicated that the fluorescence intensity was highest in the MIL-100@Era/L-Arg-HA group (Fig. 4B). Subsequently, we further characterized the intracellular levels of MDA and 4-HNE, which are products of cellular metabolism of lipid ROS and markers of ferroptosis [44,45]. As shown in Fig. 4C and D, after treatment with the nanoplatforms, the intracellular levels of MDA and 4-HNE significantly increased, with the highest levels observed in the MIL-100@Era/L-Arg-HA group. To further characterize the changes in

MDA and 4-HNE levels, we conducted Western blotting and immunofluorescence experiments. As shown in Fig. S10, consistent with the results in Fig. 4C and D, the nanoplatform significantly increased intracellular MDA and 4-HNE levels, with the highest MDA level observed after MIL-100@Era/L-Arg-HA treatment. The immunofluorescence staining results showed the same trend (Fig. S11). To further characterize the distribution of lipid ROS within cells, we used CLSM. As shown in Fig. 4F, after treatment with different nanoplatforms, the intracellular green fluorescence significantly increased, with the highest intensity observed in the MIL-100@Era/L-Arg-HA group. This indicates that MIL-100@Era/L-Arg-HA can induce ferroptosis in tumor cells. Additionally, the generation of lipid ROS leads to the destruction of tumor cell mitochondria, inducing cell death. We collected cell samples after different treatments and characterized the morphology of the mitochondria. As shown in Fig. 4G, the MIL-100@Era/L-Arg-HA group exhibits a marked alteration in the number and morphology of mitochondria compared to the control group. Specifically, the TEM images reveal that the MIL-100@Era/L-Arg-HA treatment led to mitochondrial shrinkage, loss of cristae, and increased mitochondrial membrane density-hallmarks of ferroptosis-induced mitochondrial damage. Additionally, a reduction in mitochondrial quantity can be observed, which suggests that ferroptosis may lead to mitochondrial degradation or impaired biogenesis. These changes indicate that MIL-100@Era/L-Arg-HA induces oxidative stress, triggering ferroptosis and resulting in significant structural alterations within mitochondria. Additionally, we quantitatively analyzed the effect of the nanoplatform on mitochondrial membrane potential after ferroptosis activation using flow cytometry. As shown in Fig. S12, after the addition of MIL-100, the mitochondrial membrane potential decreased, and JC-1 shifted from its aggregated form to the monomeric form. Following MIL-100@Era/L-Arg-HA treatment, the proportion of membrane potential reduction was the highest, indicating the most severe mitochondrial damage. This is consistent with the results observed through cellular transmission electron microscopy. The above experimental results demonstrate that MIL-100@Era/L-Arg-HA, through biocatalytic reactions, catalyzes the production of NO gas from L-Arg and, together with Fe^{3+} ions, maximally depletes intracellular GSH. The depletion of GSH, along with Erastin, increases intracellular lipid ROS levels, inducing ferroptosis in tumor cells (Fig. 4E).

2.8. Evaluation of the antitumor activity of the engineered nanoplatforms

First, we used the CCK8 assay kit to evaluate the cell viability of different concentrations of MIL-100 and Erastin. As shown in Fig. S5A, MIL-100 exhibited significant cytotoxicity when the nanoplatforms concentration was greater than 10 μg/mL. Additionally, as shown in Fig. S5B, Erastin displayed concentration-dependent cytotoxic behavior. In subsequent experiments, based on the cytotoxicity results of Erastin and the drug loading efficiency, we standardized the dosage for the following experiments: Erastin at 30 μM and the nanoplatforms at 52.6 μg/mL. To compare the antitumor activity of the differently modified nanoplatforms, we measured the cell viability after different treatments. As shown in Fig. 5A, the antitumor activity of MIL-100 increased after the introduction of Erastin and L-Arg. The addition of the HA targeting molecule resulted in MIL-100@Era/L-Arg-HA exhibiting the strongest antitumor activity, with cell viability at 36.71 % within 24 h. In contrast, the cell viability of the MIL-100 group was 76.79 %, MIL-100@L-Arg was 64.48 %, and MIL-100@Era/L-Arg was 48.7 %. To further characterize the antitumor activity of the engineered nanoplatforms, we used the Annexin V-FITC apoptosis detection kit to assess the apoptosis levels of tumor cells. As shown in Figs. 5C and 4T1 cells exhibited varying levels of apoptosis after treatment with the nanoplatforms, with a time-dependent relationship where the apoptosis level in the 24-h treatment group was significantly higher than in the 12-h group. Among them, the MIL-100@Era/L-Arg-HA group showed the highest apoptosis level, with 41.6 % apoptosis after 24 h of treatment. These results indicate that gas
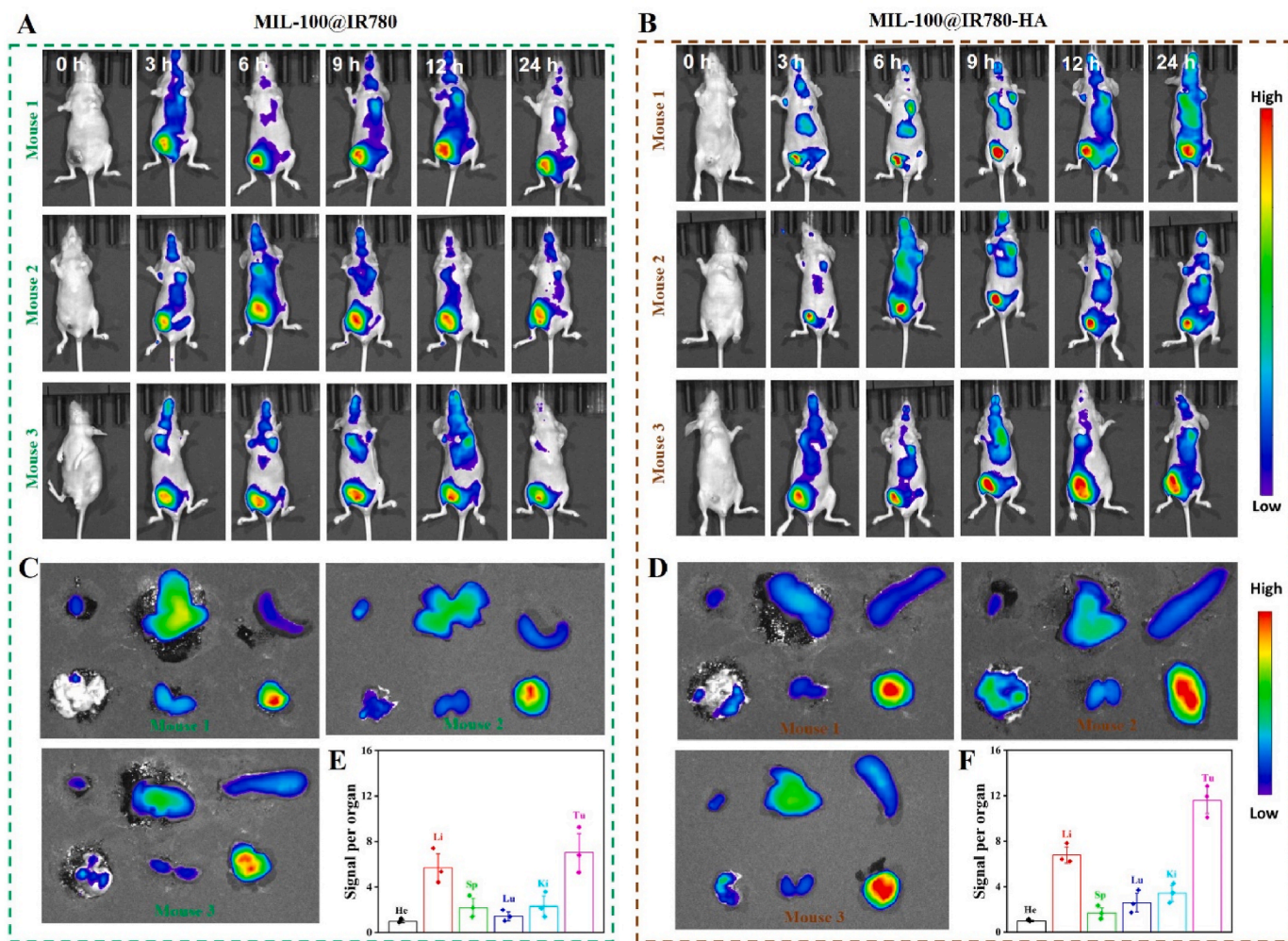
Fig. 6. *In vivo* and *in vitro* biodistribution of the engineered nanoplatform. (A, B) Fluorescence images at specified time points after intravenous injection of MIL-100@IR780 and MIL-100@IR780-HA in 4T1 tumor-bearing mice. (C, E) Fluorescence images of major organs and tumor tissues 24 h after injection of MIL-100@IR780 and MIL-100@IR780-HA. (D, F) Analysis of the average fluorescence intensity in major organs and tumor tissues (n = 3).

therapy-enhanced ferroptosis can significantly induce tumor cell death.

2.9. Evaluation of ferroptosis inhibitors on the recovery of engineered nanoplatform-mediated ferroptosis

Fer-1 (Ferrostatin-1) [46] and DFO (Deferoxamine) [47] are two commonly used inhibitors of ferroptosis, but they act through different mechanisms to inhibit iron-dependent cell death. Here, we used DFO to determine iron-mediated ferroptosis and Fer-1 to elucidate the combined effects of NO, iron, and Erastin-mediated ferroptosis. As shown in Fig. 5B, after treatment with different concentrations of DFO and Fer-1, we observed a partial recovery in cell viability induced by MIL-100@Era/L-Arg-HA, showing concentration dependence. Specifically, under the combined treatment of 120 μM DFO and 10 μM Fer-1, the cell viability of MIL-100@Era/L-Arg-HA recovered from 36.27 % to 76.79 %. Additionally, we evaluated the apoptosis levels of tumor cells mediated by MIL-100@Era/L-Arg-HA using flow cytometry after treatment with DFO and Fer-1. As shown in Figs. 5D and S6, the apoptosis rate of tumor cells mediated by MIL-100@Era/L-Arg-HA decreased from 47.1 % to 14.06 % after treatment. These experimental results confirm that gas-enhanced ferroptosis mediated by the engineered nanoplatform can significantly induce tumor cell death and can be alleviated by iron death inhibitors DFO and Fer-1.

2.10. Evaluation of various inhibitors on the recovery of engineered nanoplatform-mediated ferroptosis

To verify whether ferroptosis is the primary mechanism by which this system induces tumor cell death, we added the apoptosis inhibitor Z-VAD-FMK, the necroptosis inhibitor Necrostatin-1, and the autophagy inhibitor 3-Methyladenine. As shown in Figs. 5E and S15, after the addition of Z-VAD-FMK, the apoptosis rate of tumor cells decreased from 44.7 % to 31.7 %. This is due to oxidative stress caused by hydroxyl radicals and NO generated through the Fenton reaction in the system, which leads to caspase-dependent apoptosis in tumor cells. However, the addition of Necrostatin-1 and 3-Methyladenine did not alleviate apoptosis. In summary, ferroptosis is the main pathway through which this nanoplatform induces tumor cell death.

2.11. Evaluation of in vivo biodistribution pattern of engineered nanoplatform

To study the *in vivo* distribution of the nanoplatform, 4T1 tumor-bearing mice were intravenously injected with IR780-labeled nanoplatforms (MIL-100@IR780 and MIL-100@IR780-HA). Post-injection, fluorescence patterns at 780 nm were captured using the *IVIS* system. As shown in Fig. 6A and **B**, MIL-100@IR780-HA effectively accumulated at the tumor site, whereas MIL-100@IR780 primarily deposited in non-specific organs. After 24 h post-injection, major organs and tumors
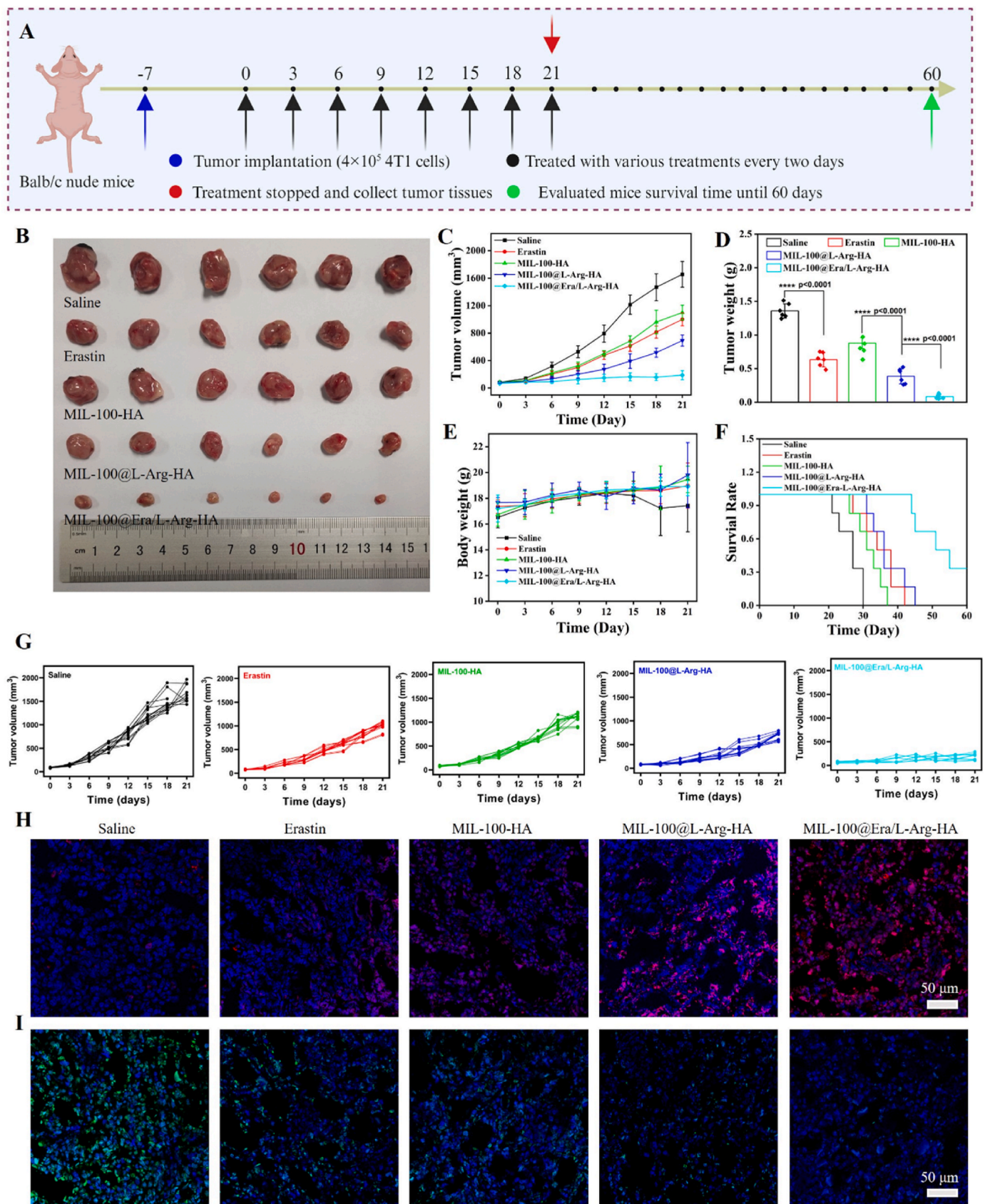
Fig. 7. Evaluation of the *in vivo* antitumor effects of the engineered nanoplatform. (A) Schematic illustration of the *in vivo* antitumor treatment. (B) Images of tumor tissues from tumor-bearing mice 21 days after different treatments (n = 6); (C) Average tumor volume growth curves over 21 days after different treatments (n = 12); (D) *Ex vivo* tumor tissue weight (n = 6); (E) Body weight changes in mice during the treatment process (n = 12); (F) Survival curves of tumor-bearing mice over 60 days; (G) Individual tumor volume growth curves over 21 days after different treatments (n = 12); (H) TUNEL staining of tumor tissues; (I) Ki67 immunofluorescence staining of tumor tissues.

were harvested for *ex vivo* imaging. As shown in Fig. 6C and **D**, MIL-100@IR780 and MIL-100@IR780-HA were highly enriched in the liver and kidneys, indicating predominant excretion pathways. Imaging results demonstrated that MIL-100@IR780-HA exhibited superior tumor-targeting efficacy compared to MIL-100@IR780 (Fig. 6E and **F**). These imaging findings indicate that MIL-100@IR780-HA accumulates in tumor tissues *via* enhanced permeability and retention (EPR) effect and HA-mediated targeting, which is benefit for *in vivo* anti-tumor therapy.

2.12. In vivo anti-tumor efficacy evaluation of the engineered nanoplatform

To evaluate the *in vivo* anti-tumor efficacy of the gas therapy-enhanced ferroptosis strategy mediated by the nanoplatform, we established a 4T1 subcutaneous tumor model. When the tumor volume reached approximately 100 mm^3, tumor-bearing mice were randomly divided into five groups (12 mice per group) and treated with saline, Erastin, MIL-100-HA, MIL-100@L-Arg-HA, or MIL-100@Era/L-Arg-HA. Treatments were administered *via* tail vein injection every two days, and the body weight and tumor volume of the mice were continuously recorded during the treatment period (Fig. 7A). After 21 days of treatment, six mice from each group were randomly selected and euthanized to obtain tumor tissue images and weights. The survival rate of the remaining six mice in each group was observed until 60 days or until the mice died. From the tumor tissue images, it was observed that the MIL-100@Era/L-Arg-HA group, which mediated gas therapy-enhanced ferroptosis, had the smallest tumor volume, followed by the MIL-100@L-Arg-HA group. Compared to the saline group, the Erastin and MIL-100-HA groups had smaller tumor volumes (Fig. 7B and **C**). The results of *in vitro* tumor tissue weight also showed that the MIL-100@Era/L-Arg-HA group had the smallest tumor weight (Fig. 7D). Additionally, the survival curves of the mice confirmed that the MIL-100@Era/L-Arg-HA group had the longest survival time, indicating that this group could effectively inhibit the growth of tumor cells *in vivo* and extend the survival time of the mice (Fig. 7F).

To further verify the impact of the gas therapy-enhanced ferroptosis strategy mediated by the engineered nanoplatform on tumor tissues, we prepared frozen sections of freshly obtained tumor tissues and conducted immunofluorescence experiments to detect the expression of relevant proteins in the tumor tissues. Firstly, TUNEL staining was performed on the obtained frozen sections. As shown in Fig. 7H, the MIL-100@Era/L-Arg-HA group exhibited the highest fluorescence intensity compared to the other groups. This indicates that the gas therapy-enhanced ferroptosis strategy mediated by the engineered nanoplatform can effectively induce tumor cell apoptosis, thereby inhibiting the growth of tumor tissues. Next, we conducted immunofluorescence experiments on the Ki67 protein in the tumor tissues (Fig. 7I). The results showed that the MIL-100@Era/L-Arg-HA group exhibited the lowest green fluorescence, indicating the lowest cell viability in this group. This trend is consistent with the TUNEL staining results, confirming that the tumor volume grew the slowest after treatment in the strategy group. In summary, we demonstrated that the nanoplatform can specifically accumulate at the tumor site through the EPR effect and HA targeting. Finally, the gas therapy-enhanced ferroptosis strategy mediated by the engineered nanoplatform can kill tumor cells and inhibit their proliferative activity.

The *in vivo* biocompatibility of nanomaterials is a critical factor in assessing their clinical potential. First, we collected blood samples from mice to conduct hemolysis tests, evaluating the biosafety of the nanoplatform during the *in vivo* treatment process. As shown in Fig. S16, the MIL-100-HA, MIL-100@L-Arg-HA, and MIL-100@Era/L-Arg-HA groups exhibited good biocompatibility, with no observed hemolysis. Additionally, the body weight curves of tumor-bearing mice during the treatment confirmed that the nanoplatforms were non-toxic, as they did not cause weight loss. The H&E staining results of the major organs in

tumor-bearing mice also confirmed that after the injection of the nanoplatform, no significant toxic side effects were observed in the main organs (Fig. S17). All the above experimental results demonstrate that the engineered nanoplatforms possess good biosafety *in vivo* and do not induce significant toxic side effects in mice, indicating their potential for future clinical applications.

3. Conclusion

In this study, we designed and developed an engineered nanoplatform that enhances ferroptosis through gas therapy. This nanoplatform integrates the ferroptosis activator Erastin, dopamine molecules for surface modification, L-Arg for catalytic activity, and hyaluronic acid (HA) for tumor targeting to enhance the induction of ferroptosis. After the HA-mediated nanoplatform is targeted and taken up by tumor cells, the Fe element contained in MIL-100 undergoes valence changes between Fe^{3+} and Fe^{2+} under the action of GSH and H$_2$O$_2$. L-Arg, catalyzed by intracellular H$_2$O$_2$ and other substances, produces NO gas that reacts with GSH. Erastin inhibits the cystine/glutamate antiporter system to deplete GSH, thereby reducing cystine uptake and impairing GPX4, while also increasing intracellular H$_2$O$_2$ levels by activating NOX4 protein expression. These mechanisms work together to maximize the depletion of intracellular GSH, increase intracellular lipid reactive oxygen species levels, and activate ferroptosis. This method of gas therapy-enhanced ferroptosis shows good antitumor activity *in vitro* and significantly inhibits tumor cell growth and extends the survival time of tumor-bearing mice *in vivo*. The engineered nanoplatform-mediated gas therapy-enhanced ferroptosis holds significant potential for ferroptosis-based cancer therapy and may provide more potential treatment strategies for clinical tumor treatment.

CRediT authorship contribution statement

Kun Xu: Writing – original draft, Visualization, Investigation, Formal analysis, Data curation. **Ke Li:** Writing – review & editing, Software, Methodology, Formal analysis, Conceptualization. **Ye He:** Writing – original draft, Software, Methodology, Formal analysis. **Yulan Mao:** Writing – original draft, Methodology, Formal analysis. **Xuan Li:** Software, Methodology, Formal analysis. **Liangshuai Zhang:** Validation, Investigation, Methodology. **Meijun Tan:** Visualization, Validation, Investigation. **Yulu Yang:** Validation, Software, Investigation, Data curation. **Zhong Luo:** Validation, Supervision, Software, Methodology. **Peng Liu:** Visualization, Supervision, Methodology. **Kaiyong Cai:** Writing – review & editing, Supervision, Project administration, Funding acquisition, Conceptualization.

Ethics approval and consent to participate

All animal experiments were conducted following ethical requirements and approved by the Laboratory Animal Welfare and Ethics Committee of Chongqing University (CQU-IACUC-RE-202112-003).

Declaration of competing interest

The authors declare that they have no known competing financial interests or personal relationships that could have appeared to influence the work reported in this paper.

Acknowledgments

Appendix A. Supplementary data

Supplementary data to this article can be found online at https://doi.org/10.1016/j.bioactmat.2024.10.024.

References

[1] J. Dixon Scott, Kathryn M. Lemberg, Michael R. Lamprecht, R. Skouta, Eleina M. Zaitsev, Caroline E. Gleason, Darpan N. Patel, Andras J. Bauer, Alexandra M. Cantley, Wan S. Yang, B. Morrison, Brent R. Stockwell, Ferroptosis: an iron-dependent form of nonapoptotic cell death, Cell 149 (5) (2012) 1060–1072.

[2] S.J. Dixon, J.A. Olzmann, The cell biology of ferroptosis, Nat. Rev. Mol. Cell Biol. 25 (6) (2024) 424–442.

[3] L. Zhao, X. Zhou, F. Xie, L. Zhang, H. Yan, J. Huang, C. Zhang, F. Zhou, J. Chen, L. Zhang, Ferroptosis in cancer and cancer immunotherapy, Cancer Commun. 42 (2) (2022) 88–116.

[4] D.D. Zhang, Ironing out the details of ferroptosis, Nat. Cell Biol. 26 (2024) 1386–1393.

[5] N. Kang, S. Son, S. Min, H. Hong, C. Kim, J. An, J.S. Kim, H. Kang, Stimuli-responsive ferroptosis for cancer therapy, Chem. Soc. Rev. 52 (12) (2023) 3955–3972.

[6] Y. Xiong, C. Xiao, Z. Li, X. Yang, Engineering nanomedicine for glutathione depletion-augmented cancer therapy, Chem. Soc. Rev. 50 (10) (2021) 6013–6041.

[7] S. Wang, F. Li, R. Qiao, X. Hu, H. Liao, L. Chen, J. Wu, H. Wu, M. Zhao, J. Liu, R. Chen, X. Ma, D. Kim, J. Sun, T.P. Davis, C. Chen, J. Tian, T. Hyeon, D. Ling, Arginine-rich manganese silicate nanobubbles as a ferroptosis-inducing agent for tumor-targeted theranostics, ACS Nano 12 (12) (2018) 12380–12392.

[8] J. Hu, J. Zhu, K. Wang, X. Yan, L. Xu, X. Zhang, H. Ding, P. Yang, S. Hu, R. Xie, Engineered-doping strategy for self-sufficient reactive oxygen species blossom to amplify ferroptosis/cuproptosis sensibilization in hepatocellular carcinoma treatment, Advanced Functional Materials n/ a (n/a) (2024) 2405383.

[9] L. Zeng, S. Ding, Y. Cao, C. Li, B. Zhao, Z. Ma, J. Zhou, Y. Hu, X. Zhang, Y. Yang, G. Duan, X.-w. Bian, G. Tian, A MOF-based potent ferroptosis inducer for enhanced radiotherapy of triple negative breast cancer, ACS Nano 17 (14) (2023) 13195–13210.

[10] M. Hou, M. Liu, H. Yu, Y. Kou, J. Jia, Q. Zhou, F. Zhang, D. Zhao, T. Zhao, X. Li, Spatially asymmetric nanoparticles for boosting ferroptosis in tumor therapy, Nano Lett. 24 (4) (2024) 1284–1293.

[11] Z. Rao, Y. Xia, Q. Jia, Y. Zhu, L. Wang, G. Liu, X. Liu, P. Yang, P. Ning, R. Zhang, X. Zhang, C. Qiao, Z. Wang, Iron-based metal-organic framework co-loaded with buthionine sulfoximine and oxaliplatin for enhanced cancer chemo-ferrotherapy via sustainable glutathione elimination, J. Nanobiotechnol. 21 (1) (2023) 265.

[12] K. Li, K. Xu, Y. He, L. Lu, Y. Mao, P. Gao, G. Liu, J. Wu, Y. Zhang, Y. Xiang, Z. Luo, K. Cai, Functionalized tumor-targeting nanosheets exhibiting Fe(II) overloading and GSH consumption for ferroptosis activation in liver tumor, Small 17 (40) (2021) 2102046.

[13] Q. Fan, W. Xiong, H. Zhou, J. Yang, J. Feng, Z. Li, L. Wu, F. Hu, X. Duan, B. Li, J. Fan, Y. Xu, X. Chen, Z. Shen, An and logic gate for magnetic-resonance-imaging-guided ferroptosis therapy of tumors, Adv. Mater. 35 (45) (2023) 2305932.

[14] X. Dai, Y. Zhu, M. Su, J. Chen, S. Shen, C.-F. Xu, X. Yang, Rigid shell decorated nanodevice with Fe/H_2O_2 supply and glutathione depletion capabilities for potentiated ferroptosis and synergized immunotherapy, Adv. Funct. Mater. 33 (27) (2023) 2215022.

[15] H. Xu, D. Ye, M. Ren, H. Zhang, F. Bi, Ferroptosis in the tumor microenvironment: perspectives for immunotherapy, Trends Mol. Med. 27 (9) (2021) 856–867.

[16] Y. Zhou, K. Chen, W.K. Lin, J. Liu, W. Kang, Y. Zhang, R. Yang, L. Jin, Y. Cheng, A. Xu, W. Wang, Photo-enhanced synergistic induction of ferroptosis for anti-cancer immunotherapy, Adv. Healthcare Mater. 12 (27) (2023) 2300994.

[17] J. Liu, J. Zhan, Y. Zhang, L. Huang, J. Yang, J. Feng, L. Ding, Z. Shen, X. Chen, Ultrathin clay nanoparticles-mediated mutual reinforcement of ferroptosis and cancer immunotherapy, Adv. Mater. 36 (9) (2024) 2309562.

[18] K. Li, K. Xu, Y. He, Y. Yang, M. Tan, Y. Mao, Y. Zou, Q. Feng, Z. Luo, K. Cai, Oxygen self-generating nanoreactor mediated ferroptosis activation and immunotherapy in triple-negative breast cancer, ACS Nano 17 (5) (2023) 4667–4687.

[19] K. Li, K. Xu, S. Liu, Y. He, M. Tan, Y. Mao, Y. Yang, J. Wu, Q. Feng, Z. Luo, K. Cai, All-in-One engineering multifunctional nanoplatforms for sensitizing tumor low-temperature photothermal therapy in vivo, ACS Nano 17 (20) (2023) 20218–20236.

[20] P. Liao, W. Wang, W. Wang, I. Kryczek, X. Li, Y. Bian, A. Sell, S. Wei, S. Grove, J. K. Johnson, P.D. Kennedy, M. Gijón, Y.M. Shah, W. Zou, CD8+ T cells and fatty acids orchestrate tumor ferroptosis and immunity via ACSL4, Cancer Cell 40 (4) (2022) 365–378.e6.

[21] Y. Zhang, K. Zhang, H. Yang, Y. Hao, J. Zhang, W. Zhao, S. Zhang, S. Ma, C. Mao, Highly penetrable drug-loaded nanomotors for photothermal-enhanced ferroptosis treatment of tumor, ACS Appl. Mater. Interfaces 15 (11) (2023) 14099–14110.

[22] W. Cao, M. Sun, K.N. Yu, L. Zhao, Y. Feng, C. Tan, M. Yang, Y. Wang, F. Zhu, L. Chen, L. Nie, Y. Zhao, G. Chen, W. Han, Exogenous carbon monoxide promotes GPX4-dependent ferroptosis through ROS/GSK3β axis in non-small cell lung cancer, Cell Death Discovery 10 (1) (2024) 42.

[23] Y. Zhang, L. Wang, L. Liu, L. Lin, F. Liu, Z. Xie, H. Tian, X. Chen, Engineering metal–organic frameworks for photoacoustic imaging-guided chemo-/photothermal combinational tumor therapy, ACS Appl. Mater. Interfaces 10 (48) (2018) 41035–41045.

[24] S. Sheng, F. Liu, L. Lin, N. Yan, Y. Wang, C. Xu, H. Tian, X. Chen, Nanozyme-mediated cascade reaction based on metal-organic framework for synergetic chemo-photodynamic tumor therapy, J. Contr. Release 328 (2020) 631–639.

[25] X. Wan, L. Song, W. Pan, H. Zhong, N. Li, B. Tang, Tumor-targeted cascade nanoreactor based on metal-organic frameworks for synergistic ferroptosis–starvation anticancer therapy, ACS Nano 14 (9) (2020) 11017–11028.

[26] W. Fan, N. Lu, P. Huang, Y. Liu, Z. Yang, S. Wang, G. Yu, Y. Liu, J. Hu, Q. He, J. Qu, T. Wang, X. Chen, Glucose-Responsive sequential generation of hydrogen peroxide and nitric oxide for synergistic cancer starving-like/gas therapy, Angew. Chem. Int. Ed. 56 (5) (2017) 1229–1233.

[27] Z. Yuan, C. Lin, Y. He, B. Tao, M. Chen, J. Zhang, P. Liu, K. Cai, Near-infrared light-triggered nitric-oxide-enhanced photodynamic therapy and low-temperature photothermal therapy for biofilm elimination, ACS Nano 14 (3) (2020) 3546–3562.

[28] S. Sheng, L. Lin, F. Liu, Y. Zhang, C. Xu, K. Hao, D. Wang, H. Tian, X. Chen, Endogenous biocatalytic reaction-based nanoplatform for multifunctional tumor theranostics, Chem. Mater. 34 (19) (2022) 8664–8674.

[29] T. Xue, C. Xu, Y. Wang, Y. Wang, H. Tian, Y. Zhang, Doxorubicin-loaded nanoscale metal–organic framework for tumor-targeting combined chemotherapy and chemodynamic therapy, Biomater. Sci. 7 (11) (2019) 4615–4623.

[30] D. Sang, K. Wang, X. Sun, Y. Wang, H. Lin, R. Jia, F. Qu, NIR-driven intracellular photocatalytic O_2 evolution on Z-scheme Ni_3S_2/$Cu1.8S$@HA for hypoxic tumor therapy, ACS Appl. Mater. Interfaces 13 (8) (2021) 9604–9619.

[31] N.N. Rahbari, D. Kedrin, J. Incio, H. Liu, W.W. Ho, H.T. Nia, C.M. Edrich, K. Jung, J. Daubriac, I. Chen, T. Heishi, J.D. Martin, Y. Huang, N. Maimon, C. Reissfelder, J. Weitz, Y. Boucher, J.W. Clark, A.J. Grodzinsky, D.G. Duda, R.K. Jain, D. Fukumura, Anti-VEGF therapy induces ECM remodeling and mechanical barriers to therapy in colorectal cancer liver metastases, Sci. Transl. Med. 8 (360) (2016) 360ra135, 360ra135.

[32] H. Xia, M. Hao, K. Li, X. Chen, L. Yu, J. Qiu, H. Zhang, H. Li, Y. Sang, H. Liu, CD44 and HAP-conjugated hADSCs as living materials for targeted tumor therapy and bone regeneration, Adv. Sci. 10 (2) (2023) 2206393.

[33] C.-S. Lin, S.-H. Lee, H.-S. Huang, Y.-S. Chen, M.-C. Ma, H_2O_2 generated by NADPH oxidase 4 contributes to transient receptor potential vanilloid 1 channel-mediated mechanosensation in the rat kidney, Am. J. Physiol. Ren. Physiol. 309 (4) (2015) F369–F376.

[34] L. Plecitá-Hlavatá, M. Jabůrek, B. Holendová, J. Tauber, V. Pavluch, Z. Berková, M. Cahová, K. Schröder, R.P. Brandes, D. Siemen, P. Ježek, Glucose-stimulated insulin secretion fundamentally requires H_2O_2 signaling by NADPH oxidase 4, Diabetes 69 (7) (2020) 1341–1354.

[35] R. Zhou, Y. Chen, S. Li, X. Wei, W. Hu, S.a. Tang, J. Ding, W. Fu, H. Zhang, F. Chen, W. Hao, Y. Lin, R. Zhu, K. Wang, L. Dong, Y. Zhao, X. Feng, F. Chen, C. Ding, W. Hu, TRPM7 channel inhibition attenuates rheumatoid arthritis articular chondrocyte ferroptosis by suppression of the PKCα-NOX4 axis, Redox Biol. 55 (2022) 102411.

[36] O.-S. Kwon, E.-J. Kwon, H.-J. Kong, J.-Y. Choi, Y.-J. Kim, E.-W. Lee, W. Kim, H. Lee, H.-J. Cha, Systematic identification of a nuclear receptor-enriched predictive signature for erastin-induced ferroptosis, Redox Biol. 37 (2020) 101719.

[37] I. Ingold, C. Berndt, S. Schmitt, S. Doll, G. Poschmann, K. Buday, A. Roveri, X. Peng, F. Porto Freitas, T. Seibt, L. Mehr, M. Aichler, A. Walch, D. Lamp, M. Jastroch, S. Miyamoto, W. Wurst, F. Ursini, E.S.J. Arnér, N. Fradejas-Villar, U. Schweizer, H. Zischka, J.P. Friedmann Angeli, M. Conrad, Selenium utilization by GPX4 is required to prevent hydroperoxide-induced ferroptosis, Cell 172 (3) (2018) 409–422.e21.

[38] F. Ursini, M. Maiorino, Lipid peroxidation and ferroptosis: the role of GSH and GPx4, Free Radic. Biol. Med. 152 (2020) 175–185.

[39] C. Zhou, Y. Zhao, M. Yang, W. Yin, Y. Li, Y. Xiao, Y. Liu, M. Lang, Diselenide-containing polymer based on new antitumor mechanism as efficient GSH depletion agent for ferroptosis therapy, Adv. Healthcare Mater. 13 (17) (2024) 2303896.

[40] S. Zhi, X. Zhang, J. Zhang, X.-y. Wang, S. Bi, Functional nucleic acids-engineered bio-barcode nanoplatforms for targeted synergistic therapy of multidrug-resistant cancer, ACS Nano 17 (14) (2023) 13533–13544.

[41] X. Hu, R. Li, W. Wu, K. Fang, Z. Zhu, Y. Wang, L. Zhou, M. Chen, C. Dong, S. Shi, A Fe(III)-porphyrin-oxaliplatin(IV) nanoplatform for enhanced ferroptosis and combined therapy, J. Contr. Release 348 (2022) 660–671.

[42] Z. Zhou, H. Liang, R. Yang, Y. Yang, J. Dong, Y. Di, M.J.A.C. Sun, Glutathione Depletion-induced activation of dimersomes for potentiating the ferroptosis and immunotherapy of "cold", Tumor 134 (22) (2022) e202202843.

[43] Y. Li, N. Lei, X. Yao, Y. Zhang, Y. Dong, J. Yi, X. Li, W. Deng, G. Nie, Z.J.A.F.M. Qin, Hijacking endogenous iron and GSH via a polyvalent ferroptosis agonist to enhance tumor immunotherapy 33 (44) (2023) 2303195.

[44] K. Li, C. Lin, M. Li, K. Xu, Y. He, Y. Mao, L. Lu, W. Geng, X. Li, Z.J.A.n. Luo, Multienzyme-like reactivity cooperatively impairs glutathione peroxidase 4 and ferroptosis suppressor protein 1 pathways in triple-negative breast cancer for sensitized ferroptosis therapy 16 (2) (2022) 2381–2398.

[45] K. Li, C. Lin, Y. He, L. Lu, K. Xu, B. Tao, Z. Xia, R. Zeng, Y. Mao, Z.J.A.n. Luo, Engineering of cascade-responsive nanoplatform to inhibit lactate efflux for enhanced tumor chemo-immunotherapy 14 (10) (2020) 14164–14180.

[46] G. Miotto, M. Rossetto, A. Roveri, R. Venerando, A.-M. Vučković, M.L. Di Paolo, V. Bosello-Travain, M. Zaccarin, M. Maiorino, S.J.F.R.B. Toppo, Medicine, Insight the Mechanism of Ferroptosis Inhibition by Ferrostatin-1, vol. 120, 2018, pp. S120–S121.

[47] X. Yao, Y. Zhang, J. Hao, H.-Q. Duan, C.-X. Zhao, C. Sun, B. Li, B.-Y. Fan, X. Wang, W.-X. Li, Deferoxamine promotes recovery of traumatic spinal cord injury by inhibiting ferroptosis 14 (3) (2019) 532–541.